

# EFFECTS OF SHORT-TIME AUSTENITIZATION ON MECHANICAL PROPERTIES AND TRANSFORMATION-INDUCED PLASTICITY IN ALLOYED AUSTEMPERED DUCTILE IRON

**Burak Nalcaci** , **Omer Sahin**  and **Mehmet Erdogan** 

Department of Metallurgical and Materials Engineering, Faculty of Technology, Gazi University, Teknikokullar, 06560 Ankara, Turkey

**Onur Okur** 

Department of Metallurgical and Materials Engineering, Faculty of Architecture and Engineering, Kirikkale University, Yahsihan, 71450 Kirikkale, Turkey

**Murat Aydin** 

ESTAS Camshaft Company, Seyh Samil OSB Mah, Halis Vermezoglu Cad. No: 57, 58030 Sivas, Turkey

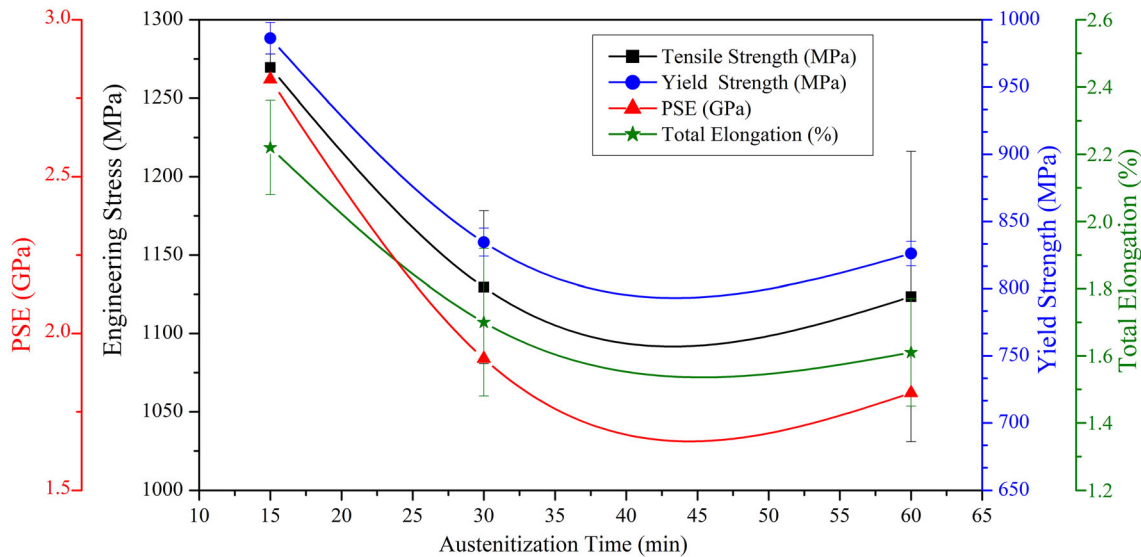
Copyright © 2021 American Foundry Society, corrected publication 2023  
<https://doi.org/10.1007/s40962-021-00723-3>

## Abstract

*The present study was performed to investigate the influences of short-time austenitization on mechanical properties and transformation-induced plasticity (TRIP) in austempered ductile iron. For this purpose, Cu–Ni–Mo-alloyed ductile iron (DI) were poured into sand molds and subsequently the DI samples were austenitized at 850 °C for the duration of 15–30–60 min followed by holding in a salt bath at an austempering temperature of 260 °C for 90 min. Characterization studies were carried out with dilatometer, image analyses software, tensile test, hardness test, XRD analysis, optical and scanning electron microscopies. Findings revealed that as the austenitization time*

*increased, carbon content of austenite (total of high carbon and blocky) and bainitic ferrite cell size enhanced, and phase volume fractions of transformation products of austenite changed. Within this context, changes in the mechanical properties were discussed. Optimum combination of strength and ductility and maximum TRIP effect were determined in the shortest (15 min)-austenitized sample. Accordingly, it was determined 15 min austenitization led to progression in the mechanical properties as 146 MPa and 0.6 % increment in the tensile strength and total elongation respectively, compared to 60 min austenitized sample.*

## Graphical Abstract



**Keywords:** austempered ductile iron (ADI), short-time austenitization, mechanical properties, transformation-induced plasticity (TRIP)

## Introduction

Austempered ductile iron (ADI) has been used in many engineering areas, including automotive components, railways, agricultural machinery, and in other industries due to its advantages such as being a favorable combination of high strength and toughness, providing design flexibility, low production cost, and relatively low density.<sup>1-5</sup> The production of ADI is provided by a casting of ductile iron (DI) alloyed according to the mechanical properties requested and austempering process.

Chemical composition of a casting should be designed precisely to acquire sound casting with high count of well-shaped spheroids in a desired matrix without intercellular carbides. In that regard, as much as amount of carbon (C) and silicon (Si) have importance, main alloying elements copper (Cu), nickel (Ni), and molybdenum (Mo) have impact on both mechanical properties and microstructure especially for heavy section parts because of enhancing austemperability (tendency to form ausferritic structure).<sup>6</sup> The addition and amount of alloying elements Cu, Ni, and Mo into ADI differ austemperability and hardenability of ductile iron and is consequently reflected in austempering kinetics and processing windows.<sup>6</sup> Austenite stabilizers elements Cu and Ni having low affinity to carbon retard the formation of carbide and overlap process windows.<sup>7</sup> This accounts for their contribution to ductility. And also, it was reported that Ni

contents up to 1% (wt.) increased the tensile strength and hardness, particularly for ADI with low ausferritic structure.<sup>8</sup> However, in the present literature, Cu has no notable influence on tensile properties except progressively increasing elongation with enhancing amount was informed for ductile iron austempered at low temperature.<sup>9,10</sup> Mo being a ferrite stabilizer element is the strongest element to improve the hardenability in ductile iron. However, its amount over 0.3% (wt.) cause to segregation in eutectic cell boundaries together with inappropriate matrix for austemperability and carbide formation.<sup>6</sup> It was acknowledged that molybdenum rich carbides serve as crack propagation paths in the earlier studies as well.<sup>11,12</sup>

DI goes through two-stage phase transformations during the austempering process. Austempering process of DI begins with the heating of cast iron in the austenitization temperature range, followed by rapid cooling in a salt bath at a temperature between 250 and 400 °C. It is then held isothermally in this range for a time required for the austempering reaction to occur. In the first stage, austenite ( $\gamma$ ) transforms into bainitic ferrite ( $\alpha_b$ ) and high-carbon austenite ( $\gamma_{hca}$ ).<sup>13</sup>



In the second stage, high-carbon austenite decomposes into carbide and ferrite ( $\alpha$ ).<sup>13</sup>



The formation of carbide in the second stage degrades the mechanical properties.<sup>14,15</sup> Therefore, in ADI, the optimum properties are obtained between Stage I and Stage II. This interval is called process window or useful range.<sup>16–18</sup>

Volume fraction, morphology, and stability of austenite (high carbon and blocky) are changed depending on austempering variables, and together with bainitic ferrite, they affect the mechanical properties significantly.<sup>19–22</sup> Austenitization temperature and time are two critical factors having importance in determining mechanical properties of ADI just as other variables like chemical composition, austempering time and temperature owing to their effects on the carbon content of primary austenite. Austenitization time determines the percentage of carbon dissolved in the austenite which in turn, affects primarily transformation kinetics and accordingly rate of phase volume fraction, phase morphology.<sup>23,24</sup> Gorny et al.<sup>25</sup> reported a similar assessment that the holding time during austenitization affected the carbon saturation in austenite, and this increase occurred most extensively at the initial stage of austenitization.

The austenitization temperature and time should be selected to enable sufficient carbon transfer from the graphite nodules (or other carbon resources like pearlite, ferrite) to the austenite matrix.<sup>26,27</sup> As the carbon solution process is both time and temperature-dependent,<sup>26</sup> while low austenitization temperatures enhance the driving force for the transformation of austenite<sup>28</sup> and lead to refinement in the structure, decreasing austenitization time shows the same trend on the driving force, resulting in attractive mechanical properties.<sup>11,29</sup> Another advantage of short-time austenitization is undoubtedly the production cost of ADI.

In a study by Batra et al.,<sup>24</sup> it was acknowledged that the austempered structure consisted of bainitic ferrite and high carbon austenite and its carbon content was non-uniform when austempered after 90 min of austenitization at 850 °C of ten mm thickness sample. When austenitization was increased to 120 min, the bainitic ferrite and retained austenite were distributed more uniformly owing to the homogeneous carbon content of austenite in the matrix.

**Table 1. Chemical Composition of ADI Used in This Study (weight%)**

C	Si	Mn	P	S	Ti	Ce
3.51	2.42	0.202	0.049	0.015	0.016	0.005
Cr	Ni	Mo	Cu	Al	Mg	Fe
0.044	1.007	0.189	0.526	0.003	0.044	Balance

Transformation-induced plasticity (TRIP) was revealed at the beginning of 1970. The TRIP effect was observed as enhancing strength and elongation due to the transformation of austenite into martensite at the time of deformation especially in the steel including retained austenite (unstable or blocky)<sup>30</sup> that had lower carbon content compared to high carbon austenite in ADI.<sup>31</sup>

In previous studies, while a group of researchers asserted the austenite in ADI was mechanically unstable,<sup>32,33</sup> austenitization temperature and time other researchers<sup>34,35</sup> suggested no such deformation-induced martensite transformation. It is known that the stability of austenite depends on its carbon content, morphology, and phases surrounding it<sup>4,33,36</sup> and is decisive in taking place of the TRIP effect and tailoring mechanical properties.<sup>37–39</sup>

Earlier researchers reported that if unstable austenite apart from high carbon austenite exists in the microstructure of ADI, unstable austenite can turn into martensite; in other words, TRIP effect could be seen in ADI just like in steel.<sup>4,13,21,39</sup>

Many studies<sup>23,40,41</sup> have investigated the effects of austempering time and temperature on ductile iron with various matrix structures. However, in the current ADI literature, no attempt has been observed to clarify the effect of short-time austenitization on TRIP and mechanical properties so far. Therefore, the present study was designed to reveal the effects of short-time austenitization on mechanical properties and TRIP in ADI. Ductile iron samples were austenitized at 850 °C for periods ranging from 15–60 minutes and immersed into a salt bath at 260 °C for 90 min. Detailed characterizations were carried out with dilatometer, image analyses software, tensile test, hardness test, XRD analysis, optical and electron microscope and presented.

## Experimental Study

### Materials

The chemical composition of ADI utilized in the present study is listed in Table 1.

The casting of DI was realized via a medium-frequency induction furnace (Inductotherm® brand) in a commercial foundry. The charge consisted of 50% pig iron, 40% ductile iron returns, and 10% steel scrap that was superheated to 1550 °C, tapped at 1450°C, and the teapod ladle method was utilized to treat a 500 kg melt of iron with 6–7% Mg containing ferrosilicon alloy for spheroidizing. Inoculation was then carried out with Ultraseed® Ce inoculant (Si:70–76%, Ca:0.75–1.25%, Ce: 1.5–2.0%, Al% 0.75–1.25, S and O: less than 1%, Fe: Balance) with the size of 0.2 to 0.7 mm in the amount of 0.15 wt. % in the ladle.

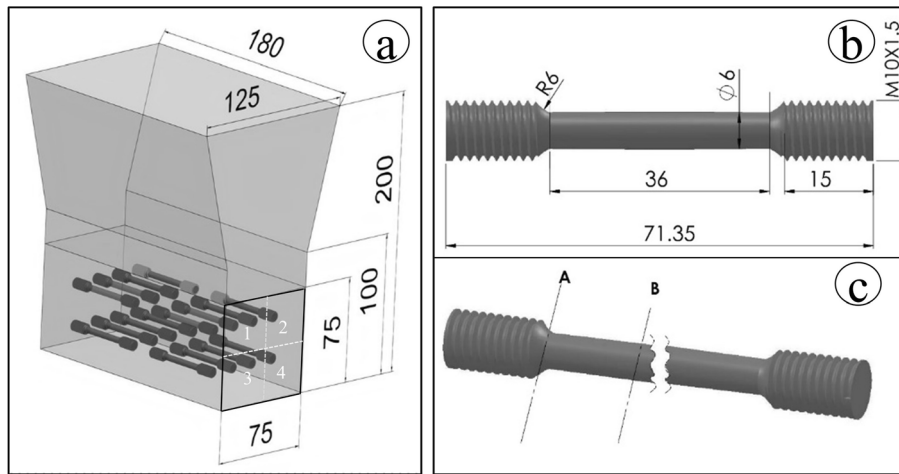


**Figure 1. (a) Dimension of Y block, (b) of tensile test sample, (c) schematic representation of the most deformed area near to fracture surface in the necked region (B section) and the least deformed area (A section) after the tensile test (dimensions are in mm).**

**Table 2. Nodularity and Nodule Counts of Graphite Spheres Depending on the Sections of Y Block**

As-Cast Samples	Section 1	Section 2	Section 3	Section 4
Nodularity (%)	86 $\pm$ 7	86 $\pm$ 5	90 $\pm$ 2	92 $\pm$ 4
Nodule counts per mm <sup>2</sup>	121 $\pm$ 6	119 $\pm$ 24	135 $\pm$ 12	143 $\pm$ 5

The chemical composition of the casting was determined through optical emission spectrometer (OES) of a chilled sample. The melt at the temperature between 1400 and 1450°C was cast into Y block green sand molds (chemically bonded with bentonite) prepared in according to ASTM A897 (thickness of 3 inc/75 mm). Y block, the last zone to solidify corresponded to the top of the block which might include casting defects as it was designed for that aim. Tensile test samples were extracted from the bottom zone (3–4 sections) as shown in Figure 1 because the 3–4 sections compared to 1–2 sections of Y block had higher nodule counts and nodularity (Table 2) and machined as per ASTM E8 (Figure 1b).

The tensile test samples were coated with commercial pure copper through electrolysis processes to prevent decarburization and oxidation during heat treatment.

To investigate the TRIP effect through microstructural changes after tensile testing, specimens were extracted from the least deformed section (A) and the most deformed section (B) of tensile test sample. Schematic representation of the section A and B on broken tensile test specimen is given in Figure 1c.

## Heat Treatments

A Baerher dilatometer was utilized to determine the  $Ac_1$ , upper critical and martensite start temperature ( $M_s$ ). The cylindrical DI samples, after full annealing at 900 °C followed by cooling to room temperature in the furnace, having a 4 mm diameter, 10 mm length, were used in the dilatometer studies. The dilatometer sample was heated up to 900°C with a heating rate of 5 °C/sec. The  $Ac_1$ , upper critical, and  $M_s$  temperatures were determined from the dilatometry test, and the results were about 788 °C and 815 °C and 197 °C respectively (Figure 2). The temperature of 850 °C was chosen as austenitization temperature since the driving force for the transformation increases with a falling austenitization temperature. Process windows were established by applying austempering process at the same temperatures (austenitization and austempering) for various times, and the appropriate holding time was determined as 90 min. That investigation is not presented here.

The austempering process was implemented by austenitization in a Heraeus electric furnace pre-set at 850 °C in the open atmosphere for various times of 15–30–60 min followed by quenching in a salt bath composed of 50%  $NaNO_3$  and 50%  $KNO_3$ . It was held at an austempering temperature of 260 °C for 90 min and then cooled to the room temperature in the still air. The austenitization and austempering times represent how many minutes the specimens were kept in the furnace and salt bath at preset temperatures. The schematic presentation of the heat treatment process is given in Figure 3.

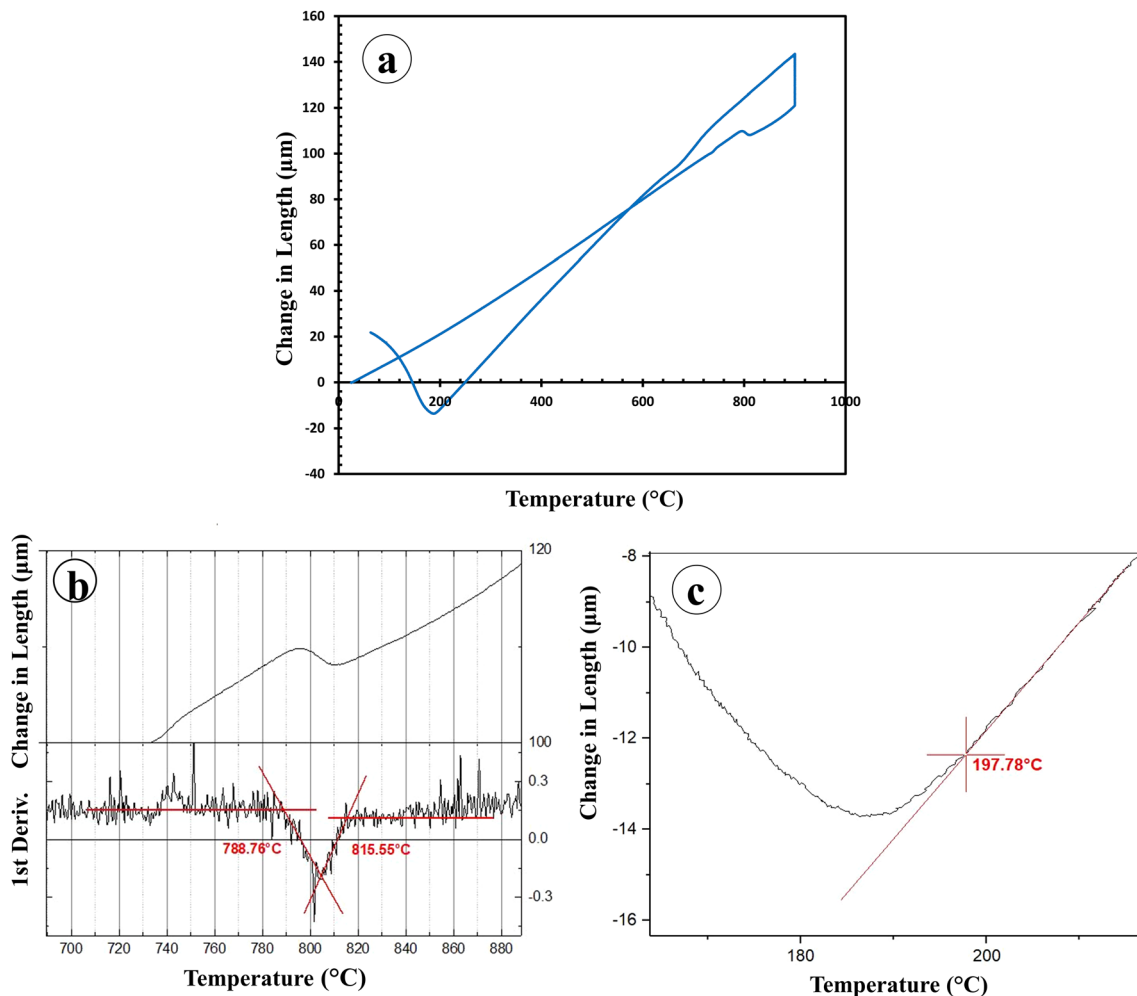


**Figure 2. The dilatation findings of the as-cast ductile iron sample; (a) Curve of Change in Length-Temp (b) Determination of  $A_{c1}$  and Upper Crit. Temp.(c) Determination of  $M_s$  Temp.**

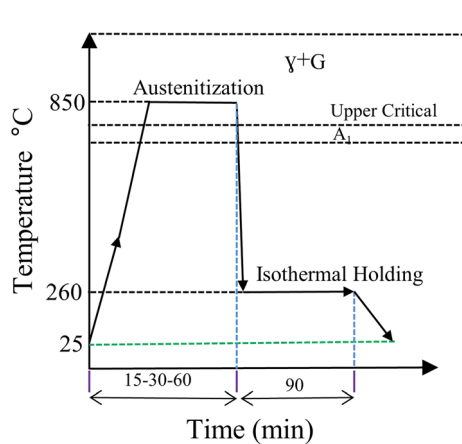


**Figure 3. Schematic presentation of the heat treatment process.**

### Materials Characterization

Tensile tests were carried out at room temperature via Instron 3369 universal testing machine with 50 kN loading capacity at a strain rate of  $0.0067 \text{ s}^{-1}$  as per ASTM E8. A

clip-on extensometer was used for the strain measurement of the gauge length at 25 mm. Three tensile samples were tested per each heat-treated condition and mean values were presented. The hardness tests were conducted in Emcotest Duravision 200 model universal hardness tester with Brinell (HBW 2.5-187.5 kgf) method. Three different indentations were performed for each heat-treated condition and their mean values were submitted.

Metallographic samples prepared from A and B sections of tensile test specimens in each heat-treated condition after a fracture are shown in Figure 1c. These samples were ground and polished up to a  $1 \mu\text{m}$  diamond suspension in accordance with standard procedures (without mounting to prevent any effects like heat on the samples) and etched with a 2% Nital. The specimens were coded according to the austempered sample, austenitization time, and sectioned area from the broken tensile test specimen, e.g. AS15-A, where AS represents the austempering, 15 represents the austenitization time, and A stands for the sectioned area from the broken tensile test specimen as shown in Figure 1c.



The microstructures of the samples were analyzed through Leica DM 5000M optical microscope connected with Leica DFC 320 digital camera and HITACHI SU5000 model scanning electron microscope. Leica Application Suite Image Analysis software (LAS) version 4.6 was used for the structural characterization of the sample in as-cast condition. The total volume fraction of high carbon austenite + blocky austenite was determined by XRD analysis. The estimations of the bainitic ferrite cell size of the samples was realized from the (110) peaks of ferrite from XRD patterns by using Scherrer equation as in previous studies.<sup>27,42,43</sup>

$$d = \frac{0.9\lambda}{\beta \cos\theta} \quad \text{Eqn. 3}$$

where  $d$  is the mean cell size,  $\lambda$  is the wave length,  $\theta$  is the Bragg angle, and  $\beta$  is full width at half maximum of the peak.

X-ray diffraction patterns were obtained on a Bruker D8 Advance X-ray diffractometer and operated at 40 kV and 40 mA using monochromatic Copper  $K\alpha$  radiation ( $\lambda=1.54056 \text{ \AA}$ ). The samples were scanned in the  $2\theta$  range of  $40\text{-}100^\circ$  at a scanning speed of  $0.05^\circ/\text{sec}$ . The integrated areas of both ferrite (200) and austenite (200) peaks were used for the calculation of the volume fraction of total austenite. The volume fraction of total austenite was calculated according to the ASTM E975 standard<sup>44</sup> by using

two peak rules. Equation 4 is utilized to calculate the volume fraction of total austenite.

$$V_\gamma = \frac{\left[ \frac{I_{\gamma(200)}}{R_{\gamma(200)}} \right]}{\left[ \frac{I_{\alpha(200)}}{R_{\alpha(200)}} + \frac{I_{\gamma(200)}}{R_{\gamma(200)}} \right]} \quad \text{Eqn. 4}$$

where  $V_\gamma$ : volume fraction of total austenite,  $I$ : integrated intensity of diffraction peak, and  $R$ -value calculated from the X-ray diffraction peak position.

The carbon content of total austenite was estimated by using Eqn. 5 from the lattice parameter of the austenite.<sup>45</sup>

$$\alpha_\gamma = 0.3548 + 0.0044C_\gamma \quad \text{Eqn. 5}$$

where  $\alpha_\gamma$  is the lattice parameter of austenite in nanometer, and  $C_\gamma$  is the carbon content of austenite (wt.%).

## Experimental Findings and Discussion

### Microstructural Analysis

Ferrite (white areas) + pearlite (brown areas) + spheroidal graphite (black areas) structures were seen in the microstructure of the ductile iron in as-cast condition (Figure 4b-c). The matrix of that consisted predominately of pearlite. The nodularity and the nodule counts were measured from 4 different sections of Y block (Figure 1a)

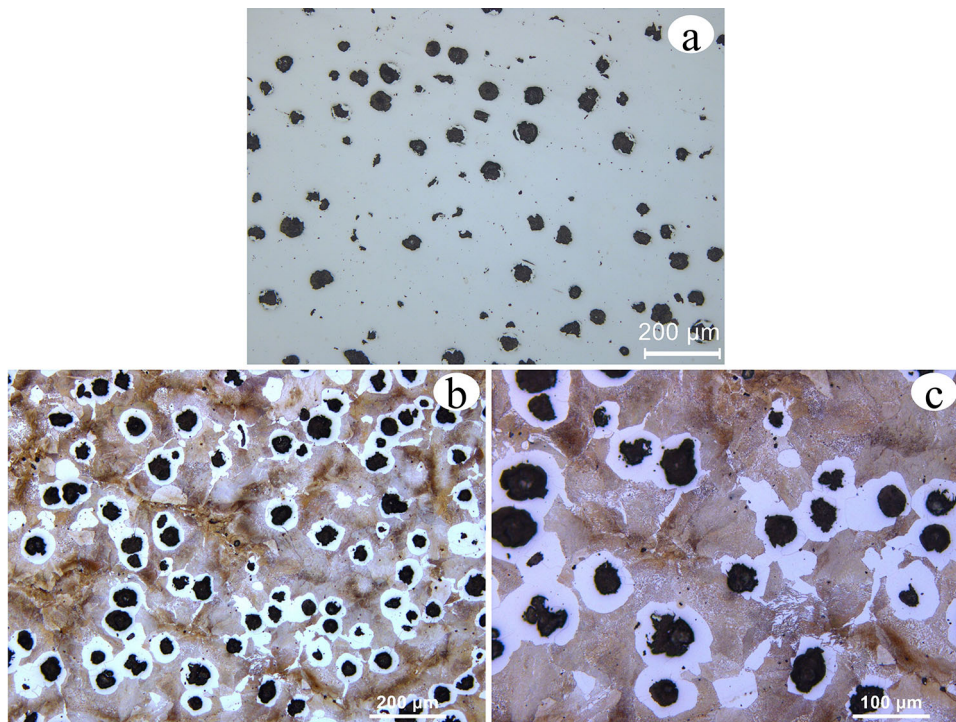


**Figure 4. Optical micrographs of the sample in as-cast condition (a) unetched, magnification: 100x (b) etched with 2% Nital, magnification: 100x (c) etched with 2% Nital, magnification: 200x.**

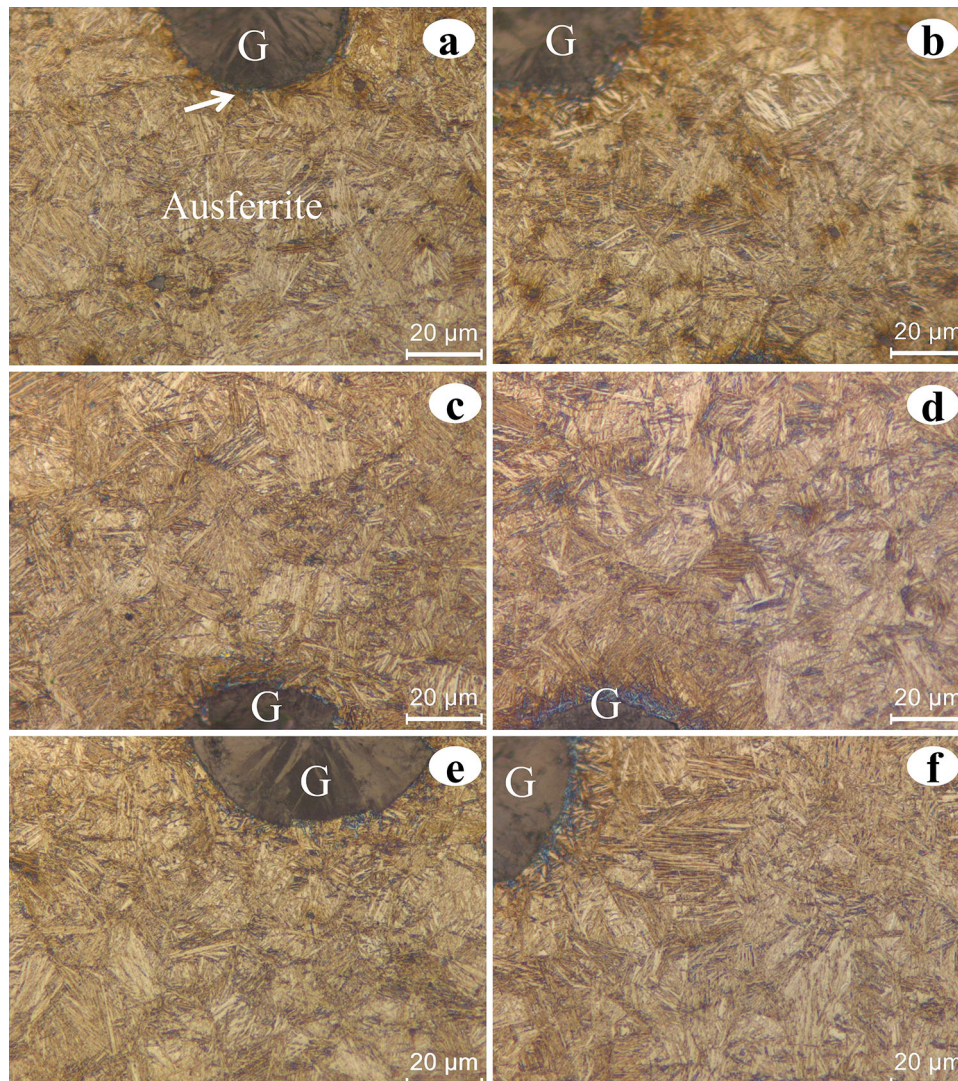


**Figure 5. Optical micrographs obtained from sections A and B of ADI broken tensile test specimens; (a) AS15-A, (b) AS15-B, (c) AS30-A, (d) AS30-B, (e) AS60-A, (f) AS60-B (Note: Arrow indicates intense ausferritic area)(Magnification: 1000x).**

according to ISO 945-4 with LAS image analyzer and presented in the Table 2. It should be noted the samples from section 1–2 was utilized only for nodularity and nodule counts calculations to disclose how they changed based on the location in Y block.

Phase volume fraction of the sample in as cast condition was calculated as graphite 16.37%, ferrite 20.34%, and pearlite 63.27% through LAS image analyzer, and its nodularity and nodule counts were found 90% and 128, respectively (Figure 4a).

Optical and SEM micrographs obtained from sections A and B of ADI broken tensile test specimens are given in Figures 5 and 6, respectively. The XRD patterns including detected phases with miller indices of all samples (including A-B section) in each heat-treated condition are illustrated in Figure 7. The microstructural constituents of

the samples are given in Table 3. The sequence of microstructural changes as a function of time determined during austempering in the present study were described in the introduction section.

As illustrated in Figure 5, the microstructures of all samples consisted of lower ausferrite structure due to low austempering temperature regardless of austenitization time.<sup>46</sup> It was noteworthy how intense and dark ausferrite was in the vicinity of the graphite (Figure 5). This is a clear evidence that graphite is significant carbon source for austenite. In an earlier study,<sup>47</sup> researchers also reported that graphite was a significant carbon source for austenite transformed from ferrite. In the continuation of the study, it was stated secondary graphitization occurred with prolonging austenitization and the secondary graphite particles caused a decrease in the ductility. Therefore, it can be said that low possibility of formation secondary



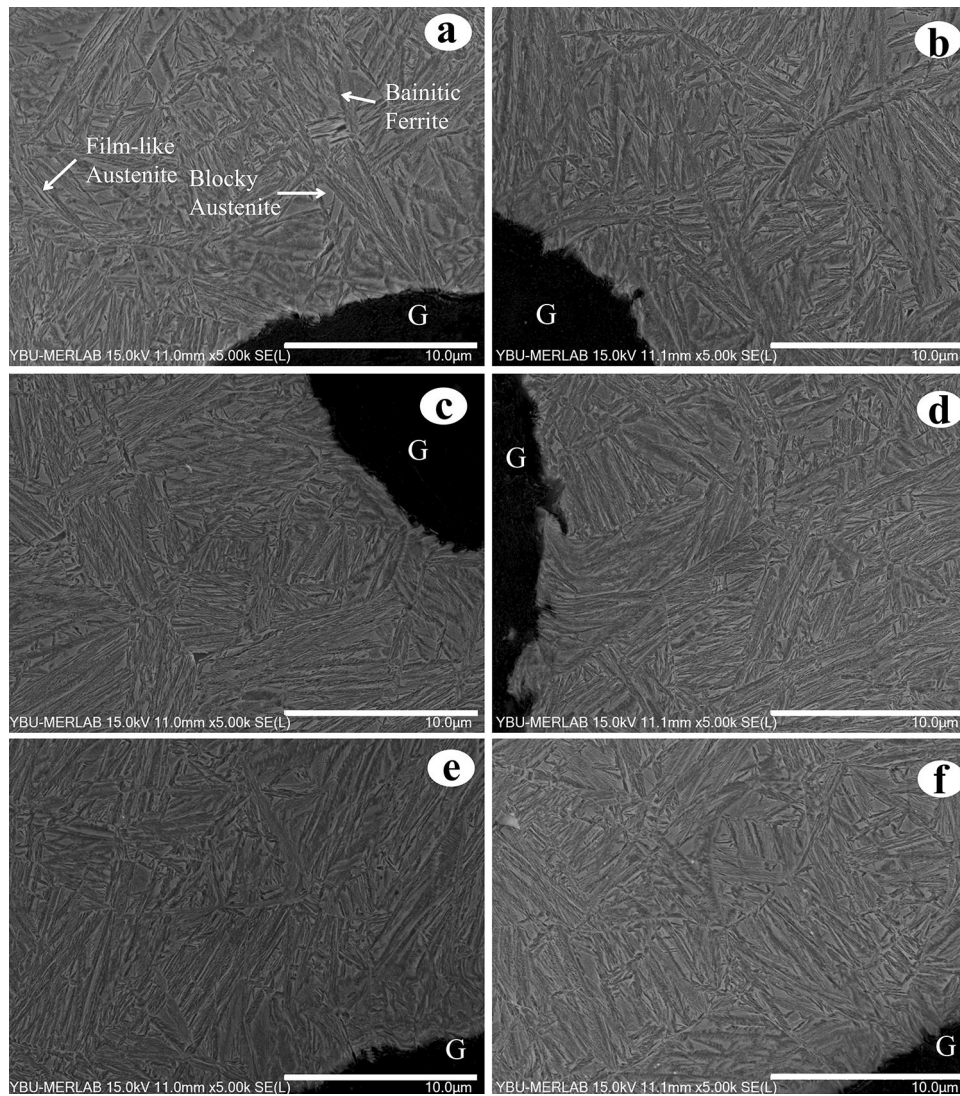


**Figure 6. SEM micrographs obtained from sections A and B of ADI broken tensile test specimens; (a) AS15-A, (b) AS15-B, (c) AS30-A, (d) AS30-B, (e) AS60-A, (f) AS60-B (Magnification: 5000x).**

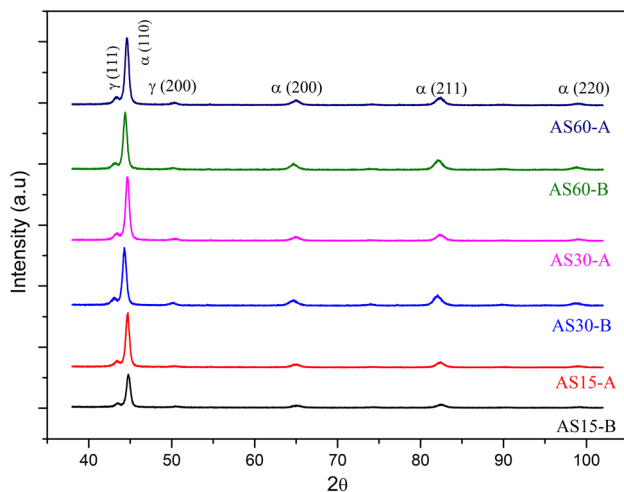


**Figure 7. XRD patterns of ADI samples.**

graphitization during short-time austenitization is another favorable impact of the process.

As illustrated in Figure 6, the microstructures of all samples were composed of blocky austenite and film-like austenite, bainitic ferrite and graphite. No morphological, microstructural differences were observed in ausferrite structures between the sections A and B taken from the same samples (Figures 5 and 6). That was very usual not to be able to distinguish any fresh-formed martensite from needle-like structure of lower ausferrite as the microstructure was very fine and similar to each other due to high driving force stemmed from low austenitization and low austempering temperatures. It is worth remembering that martensite is also high driving force-structure.

The structural changes related to austenitization time were clarified with XRD analyses.



**Table 3. Results of Metallographic Measurements**

Sample Name	Austenite *(vol. %)	Bainitic Ferrite <sup>§</sup> (vol. %)	Bainitic Ferrite Cell Size (nm)	Carbon Content in Austenite (wt.-%)	Transformation Rate <sup>tr</sup> (%)
AS15-A	17.34	82.66	14.96	1.69	11.36
AS15-B	15.37	84.63 <sup>m</sup>	–	–	–
AS30-A	18.08	81.92	16.29	1.98	4.09
AS30-B	17.34	82.66 <sup>m</sup>	–	–	–
AS60-A	18.48	81.52	17.05	2.01	4.01
AS60-B	17.74	82.26 <sup>m</sup>	–	–	–

\*Total volume fraction of austenite (high carbon and blocky austenite) calculated via XRD analysis

<sup>§</sup>Calculated via XRD analysis

<sup>–</sup>Not Calculated

<sup>m</sup>That estimations are the total value of bainitic ferrite and martensite transformed from austenite

<sup>tr</sup>Transformation rate: volume fraction of austenite of (A section–B section)/ (A section)

It should be noted in Table 3 that the bainitic ferrite volume fraction also includes martensite volume fraction, since it was not usual to separate them from each other due to familiar lattice parameters by XRD analyses.<sup>33</sup> However, a drop in the austenite volume fraction and increase in the bainitic ferrite volume fraction were distinct indicators of the phase transformation.

As can be seen from Table 3, the volume fraction of austenite increased with prolonged austenitization time and the samples acquired from section B displayed less austenite compared to the samples obtained from section A of the same sample. This behavior is related to TRIP effects. It was not possible to distinguish volume fraction of blocky austenite from total austenite. However, it is thought that the reason for the decrease at the volume fraction of austenite of A sections compared to B sections of samples were due to transformation of blocky austenite to martensite<sup>48</sup> since the blocky austenite is less

stable compared to finer austenite.<sup>37,49</sup> In addition, It is notable that blocky austenite is the primary source for martensite formation owing to inadequate carbon enrichment making the material unstable.<sup>23</sup> This result is in good agreement with the findings of previous researchers.<sup>13,50,51</sup>

It was considered the reason for the increase in the amount of austenite was correlated with the drop in driving force<sup>26</sup> depending on rising carbon solubility in austenite when the austenitization time increased. This phenomenon coincides with an investigation carried out by Batra et al.<sup>24</sup> and Lawrynowicz et al.<sup>52</sup>

The research conducted by Bayati et al.<sup>53</sup> reported that TRIP influence was observed even in austenite, with a carbon content of 1.8%, and this was related to the mechanical stability of austenite. The carbon content of the blocky austenite which is the probable region for the transformation should be less than the average carbon content of austenite.<sup>48,54,55</sup> The occurrence of the TRIP

**Table 4. The mechanical properties of all samples**

Sample Name	Yield Strength(MPa)	Eng. Tensile Strength(MPa)	Eng. Total Elongation(%)	Hardness (HBW 187.5 kgf)	PSE <sup>§</sup> GPa.%
As-cast	446.5 ± 4.3	655.2 ± 7.2	4.3 ± 0.9	232±3.24	2.8
AS-15	986.2 ± 11.7	1269.5 ± 8.5	2.21 ± 0.14	495±1.41* 501±2.70 <sup>#</sup>	2.81
AS-30	834.6 ± 10.4	1129.5 ± 48.7	1.7 ± 0.22	498.5±3.94* 499.5±4.95 <sup>#</sup>	1.92
AS-60	826.1 ± 12.1	1123.5 ± 92.6	1.61 ± 0.16	491.5±6.36* 495.5±4.99 <sup>#</sup>	1.81

\*Hardness of A section of AS15, AS30, AS60.

<sup>#</sup>Hardness of B section of AS15, AS30, AS60.

<sup>§</sup>PSE: Product of tensile strength and total elongation that was calculated by multiplication of tensile strength and total elongation.

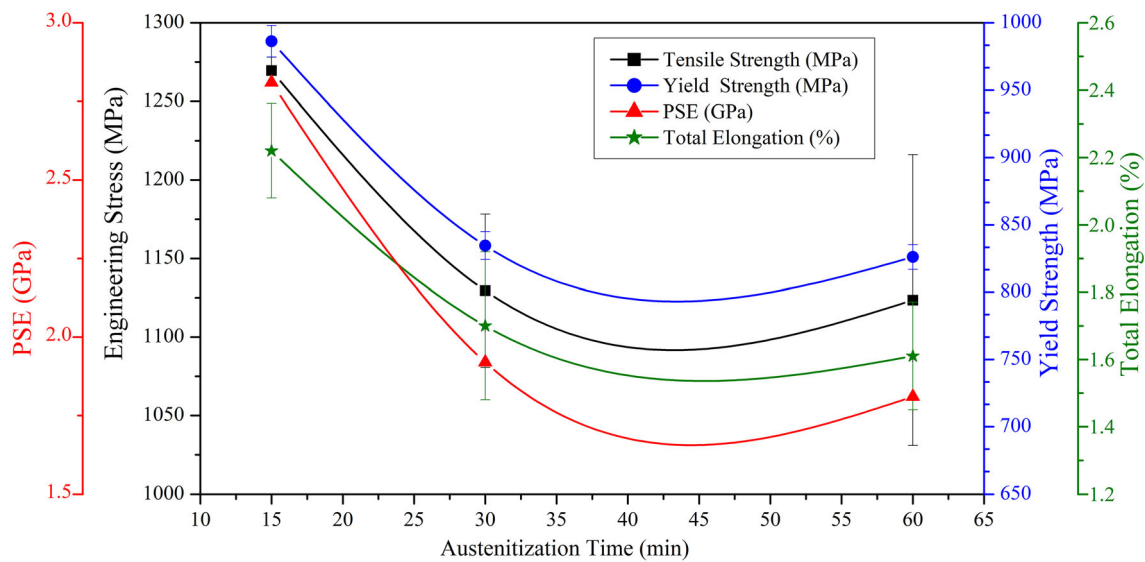


**Figure 8. Effect of austenitization time on tensile properties.**

process would require low carbon solubility in austenite linked to the stability of austenite. This is substantiated in the present work. The transformation rate (see Table 3) decreased with increasing the carbon content of austenite.

## Mechanical Properties

The mechanical properties depending on the change in the structure and the amount of phases are presented by the variations in austenitization time at the constant austempering time and temperature as the austempered structure evolves. The average values of hardness measurements, the yield and tensile strengths, and total elongations obtained for each heat treatment condition investigated are given in Table 4. Based on the mechanical test results, it could be noted that mechanical properties of the samples were directly linked to morphology (fine or coarse) of ausferrite, carbon content of austenite, phase volume fraction of the phases in the structure and contribution rate of TRIP effect.

### Hardness

The hardness of the samples acquired from the B section compared to the A sections were slightly higher for each heat-treated condition with the same austenitization times (Table 4).

This is consistent with the increase in the volume fraction of bainitic ferrite (including martensite) in Table 3, because the formation of new ferrite does not seem possible after deformation. In this case, enhancement in the total volume fraction of bainitic ferrite was probably linked to martensite formation, and this result reflected a slight increase in the hardness.

### Tensile Properties

Tensile properties of the sample in the each heat-treated condition depending on austenitization time are given in Table 4 and Figure 8.

**Yield Strength** Specimens AS-30 and AS-60 exhibited almost the same yield strength (Table 4 and Figure 8). The high value of yield strength of AS-15 can be attributable transformation of austenite due its low carbon content compared to AS-30 and AS-60 (Table 4).

**Tensile Strength** Among tested specimens for each heat treatment condition, specimen AS15 with the shortest austenitization time and the lowest carbon content in austenite exhibited the best combination of high strength and ductility (PSE) (Table 4 and Figure 8). The reasons for these favorable results were fineness of the bainitic ferrite, high amount of austenite and TRIP effect. As is well-known austenite with a low-carbon concentration helps to exhibit the TRIP effect by transforming blocky austenite into martensite during deformation. Therefore, the highest TRIP effect was determined in the AS15 sample due to low carbon concentration in austenite.<sup>43</sup> This incremental effect on ductility and strength because of TRIP was acknowledged in earlier studies.<sup>31,56</sup> However, significant carbon enrichment of austenite with prolonged austenitization time led to limited TRIP effect, along with other factors, may result in an earlier fracture. This state is more explicit between the sample AS15 with the lowest carbon content of 1.69 % and AS60 with the highest carbon content of 2.01% (Figure 8).

In the case of sample AS60, distance from the best combination of strength and ductility might be due to the detrimental effect of blocky austenite,<sup>48</sup> coarsening grain of bainitic ferrite,<sup>12</sup> lower bainitic ferrite amount,<sup>29</sup> and the limited TRIP effect due to the increased stability of austenite during prolonged austenitization (Table 3 and Table 4).

No considerable differences were observed in the mechanical properties of AS30 and AS60 due to similar metallographic measurements values as illustrated in Table 4. Therefore, it can be stated that the effect of short-time austenitization disappeared from the thirtieth minute.

**Total Elongation** In each heat-treated condition, total elongation decreased with increasing time as shown in Figure 8. Total elongation also appears to be affected by the prolonged austenitization time which led to an increase in the carbon content of austenite, lower transformation rate of austenite into martensite and coarsening of the ausferrite structure (Table 3).

## Conclusion

The effect of short-time austenitization on mechanical properties and TRIP in ADI was examined. This study reached to the following conclusions:

- 1) DI samples austenitized at 850 °C during 15–30–60 min followed by austempering at 260 °C for 90 min: Microstructures composed of high-carbon austenite, blocky austenite and bainitic ferrite were obtained in all samples.
- 2) In ADI, the TRIP effect dependent on the carbon content of austenite during austenitization was determined. The carbon content of austenite was controllable parameters linked to the time at the constant austenitization temperature.
- 3) The best combination of strength and ductility and the highest TRIP effect were determined in the sample with a 1.69 % carbon content austenitized at the shortest time (15 min) for the current study.
- 4) The amount of total austenite was increased up to 18.48%, but its transformation rate decreased from 11.36% to 4.01% with prolonged austenitization time.
- 5) When the austenitization time was extended from 15 to 60 min, while bainitic ferrite volume fraction decreased, austenite carbon solubility reached to 2.01% and bainitic ferrite cell size enhanced from 14.96 nm to 17.05 nm.
- 6) The austenitization time changing in the range of 15–60 min time resulted in a considerable improvement in the mechanical properties and

led to 146 MPa and 0.6% increment in the tensile strength and total elongation, respectively in favor of the shortest austenization time.

## Acknowledgements

The authors wish to acknowledge the financial supports of Gazi University Scientific Re-search Fund (Grant No.: GÜBAP 07/2019-19). The authors are indebted to ESTAS Camshaft Company for providing castings. Also, we would like to thank Enes Yelkovan for his help during SEM studies.

**Authors' Contributions** BN contributed to experimental studies (machining, heat treatments, mechanical tests, microstructural characterization, XRD analysis, SEM studies, investigation, creating figures, writing and editing, conceptualization). OS contributed to experimental studies (mechanical tests and microstructural characterization). OO contributed to experimental studies (microstructural characterization). MA contributed to experimental studies (casting). ME contributed to writing and editing, chemical composition design, project administration, and funding acquisition.

## Funding

This work was supported by Gazi University Scientific Research Fund (Grant No.: 07/2019-19).

## Data Availability

The raw data cannot be shared at this time as the data is also part of an ongoing study.

**Conflict of interest** The authors declare that they have no conflict of interest

## REFERENCES

1. A.D. Boccardo, P.M. Dardati, L.A. Godoy, D.J. Celentano, *Metall. Mater. Trans. B Process Metall. Mater. Process. Sci.* **49**, 1522–1536 (2018)
2. D.A. Colombo, R.C. Dommarco, A.D. Basso, *Wear* **418–419**, 208–214 (2019). <https://doi.org/10.1016/j.wear.2018.11.009>
3. S. Samaddar, T. Das, A.K. Chowdhury, M. Singh, *Mater. Today Proc.* **5**, 25615–25624 (2018). <https://doi.org/10.1016/j.matpr.2018.11.001>
4. Y. Du, X. Gao, X.X.X. Wang, X.X.X. Wang, Y. Ge, B. Jiang, *Wear* **456–457**, 203396 (2020). <https://doi.org/10.1016/j.wear.2020.203396>
5. F. Zanardi, C. Mapelli, S. Barella, *Int. J. Met.* **14**(622), 655 (2020)
6. A.S. Benam, *China Foundry.* **12**, 54–70 (2015)
7. E. Konca, K. Tur, E. Koç, *Metals (Basel)*. **7**, 1–9 (2017). <https://doi.org/10.3390/met7080320>
8. R. Elliot, *Cast Iron Technology*, 1st edn. (Butterworth, London, 1988), pp. 140–150
9. O. Erić, D. Rajnović, L. Šidjanin, S. Zec, M.T. Jovanović, *J. Serbian Chem. Soc.* **70**, 1015–1022 (2005). <https://doi.org/10.2298/JSC0507015E>



10. T. Tun, K.T. Lwin, J. Met. Mater. Miner. **18**, 199–205 (2008)
11. M. Bahmani, R. Elliott, N. Varahram, J. Mater. Sci. **32**, 4783–4791 (1997). <https://doi.org/10.1023/A:1018687115732>
12. J.O. Olawale, K.M. Oluwasegun, Mater. Perform. Charact. **5**, 20160053 (2016). <https://doi.org/10.1520/mpc20160053>
13. S. Panneerselvam, C.J. Martis, S.K. Putatunda, J.M. Boileau, Mater. Sci. Eng. A. **626**, 237–246 (2015). <https://doi.org/10.1016/j.msea.2014.12.038>
14. H. Krawiec, V. Vignal, J. Lelito, A. Krystianiak, E. Tyrała, Arch. Metall. Mater. **65**, 151–156 (2020)
15. B. Wang, G.C. Barber, C. Tao, X. Sun, X. Ran, J. Mater. Res. Technol. **7**, 198–202 (2018). <https://doi.org/10.1016/j.jmrt.2017.08.011>
16. M. Erdogan, V. Kilicli, B. Demir, J. Mater. Sci. **44**, 1394–1403 (2009). <https://doi.org/10.1007/s10853-006-1415-7>
17. V. Kilicli, M. Erdogan, Mater. Sci. Technol. **22**, 919–928 (2006). <https://doi.org/10.1179/174328406X102390>
18. I. Ovali, V. Kilicli, M. Erdogan, ISIJ Int. **53**, 375–381 (2013). <https://doi.org/10.2355/isijinternational.53.375>
19. M.X. Zhang, P.M. Kelly, L.K. Bekessy, J.D. Gates, Mater. Charact. **45**, 39–49 (2000). [https://doi.org/10.1016/S1044-5803\(00\)00044-9](https://doi.org/10.1016/S1044-5803(00)00044-9)
20. L.C. Chang, Scr. Mater. **39**, 35–38 (1998). [https://doi.org/10.1016/S1359-6462\(98\)00132-8](https://doi.org/10.1016/S1359-6462(98)00132-8)
21. X. Li, S. Soria, W. Gan, M. Hofmann, M. Schulz, M. Hoelzel, H.G. Brokmeier, W. Petry, J. Mater. Sci. **56**, 5296–5306 (2021). <https://doi.org/10.1007/s10853-020-05619-x>
22. C.Z. Wu, Y.J. Chen, T.S. Shih, Mater. Charact. **48**, 43–54 (2002). [https://doi.org/10.1016/S1044-5803\(02\)00232-2](https://doi.org/10.1016/S1044-5803(02)00232-2)
23. R. Ghasemi, I. Hassan, A. Ghorbani, A. Dioszegi, Mater. Sci. Eng. A. **767**, 138434 (2019). <https://doi.org/10.1016/j.msea.2019.138434>
24. U. Batra, S. Ray, S.R. Prabhakar, J. Mater. Eng. Perform. **12**, 426–429 (2003). <https://doi.org/10.1361/105994903770342962>
25. M. Górny, G. Angella, E. Tyrała, M. Kawalec, S. Paź, A. Kmita, Met. Mater. Int. **25**, 956–965 (2019). <https://doi.org/10.1007/s12540-019-00245-y>
26. B. Bosnjak, B. Radulovic, K. Pop-Tonev, V. Asanovic, J. Mater. Eng. Perform. **10**, 203–211 (2001). <https://doi.org/10.1361/105994901770345222>
27. L. Pereira, R.F. Do Amaral, M. Wolfart, V.K. De Barcellos, J. Mater. Res. Technol. **9**, 3055–3063 (2020)
28. A. Uyar, O. Sahin, B. Nalcaci, V. Kilicli, Int. J. Met. (2021). <https://doi.org/10.1007/s40962-021-00617-4>
29. N. Darwish, R. Elliott, Mater. Sci. Technol. (United Kingdom). **9**, 586–602 (1993). <https://doi.org/10.1179/mst.1993.9.7.586>
30. N. Saeidi, M. Jafari, J.G. Kim, F. Ashrafizadeh, H.S. Kim, Met. Mater. Int. **26**, 168–178 (2020). <https://doi.org/10.1007/s12540-019-00322-2>
31. W. Cui, M. Gintalas, P.E.J. Rivera-Diaz-del-Castillo, Mater. Sci. Eng. A. **711**, 696–703 (2018). <https://doi.org/10.1016/j.msea.2017.10.103>
32. J. Vuorinen, AFS Trans. **94**, 577 (1986)
33. X.H. Li, P. Saal, W.M. Gan, M. Hoelzel, W. Volk, W. Petry, M. Hofmann, Metall Mater. Trans. A Phys. Metall. Mater. Sci. **49**, 94–104 (2018)
34. L. Sidjanin, R.E. Smallman, S.M. Boutorabi, Mater. Sci. Technol. **10**, 711–720 (1994). <https://doi.org/10.1179/mst.1994.10.8.711>
35. L. Sidjanin, R.E. Smallman, Mater. Sci. Technol. **8**, 1095–1103 (1992). <https://doi.org/10.1179/mst.1992.8.12.1095>
36. A. Gazda, M. Warmuzek, Thermochim. Acta. **663**, 58–66 (2018). <https://doi.org/10.1016/j.tca.2018.03.010>
37. Z.P. Xiong, A.A. Saleh, R.K.W. Marceau, A.S. Taylor, N.E. Stanford, A.G. Kostryzhev, E.V. Pereloma, Acta Mater. **134**, 1–15 (2017). <https://doi.org/10.1016/j.actamat.2017.05.060>
38. H. Nasr El-Din, R. Reda, J. Mater. Eng. Perform. **28**, 2167–2177 (2019)
39. P. Parhad, V. Dakre, A. Likhite, J. Bhatt, Mater. Today Proc. **19**, 663–669 (2019). <https://doi.org/10.1016/j.matpr.2019.07.750>
40. O.E. Cekic, L. Sidjanin, D. Rajnovic, S. Balos, Met. Mater. Int. **20**, 1131–1138 (2014). <https://doi.org/10.1007/s12540-014-6017-3>
41. B. Podgornik, J. Vizintin, I. Thorbjornsson, B. Johannesson, J.T. Thorgrimsson, M. Martinez Celis, N. Valle, Wear (2012). <https://doi.org/10.1016/j.wear.2011.09.005>
42. J. Yang, S.K. Putatunda, Mater. Des. **25**, 219–230 (2004). <https://doi.org/10.1016/j.matdes.2003.09.021>
43. S.K. Putatunda, S. Kesani, R. Tackett, G. Lawes, Mater. Sci. Eng. A. **435–436**, 112–122 (2006). <https://doi.org/10.1016/j.msea.2006.07.051>
44. ASTM 975-13, *Standard Practice for X-Ray Determination of Retained Austenite in Steel with Near Random Crystallographic Orientation* (ASTM International, USA, 2003). <https://doi.org/10.1520/E0975-13>
45. C. Roberts, J. Metals **5**, 203 (1953)
46. S. Méndez, U. De La Torre, R. González-Martínez, R. Suárez, Int. J. Met. **11**, 116–122 (2017). <https://doi.org/10.1007/s40962-016-0092-9>
47. W.L. Guesser, C.L. Lopes, P.A.N. Bernardini, Int. J. Met. **14**, 717–727 (2020). <https://doi.org/10.1007/s40962-019-00397-y>
48. G. Gao, H. Guo, X. Gui, Z. Tan, B. Bai, Mater. Sci. Eng. A. **736**, 298–305 (2018). <https://doi.org/10.1016/j.msea.2018.08.091>

49. K. Dong, C. Lu, W. Zhou, D.O. Northwood, C. Liu, *Eng. Fail. Anal.* **123**, 105290 (2021). <https://doi.org/10.1016/j.engfailanal.2021.105290>
50. A.A. Nofal, H.N. El-din, M.M. Ibrahim, *Int. J. Cast Met. Res.* **20**, 47–52 (2007). <https://doi.org/10.1179/136404607X216613>
51. S. Daber, P. Prasad Rao, *J. Mater. Sci.* **43**, 357–367 (2008)
52. Z. Ławrynowicz, S. Dymski, *Arch. Foundry Eng.* **7**, 93–98 (2007)
53. H. Bayati, R. Elliott, *Int. J. Cast Met. Res.* **11**, 413–417 (1999). <https://doi.org/10.1080/13640461.1999.11819309>
54. J.K. Chen, J.S. Tsai, B.T. Chen, *Suppl. Proc. Gen. Pap. Sel.* **3**, 701–708 (2011). <https://doi.org/10.1002/9781118062173.ch89>
55. T. Jiang, H. Liu, J. Sun, S. Guo, Y. Liu, *Mater. Sci. Eng. A.* **666**, 207–213 (2016). <https://doi.org/10.1016/j.msea.2016.04.041>
56. M.M. Wang, C.C. Tasan, D. Ponge, D. Raabe, *Acta Mater.* **111**, 262–272 (2016). <https://doi.org/10.1016/j.actamat.2016.03.070>

**Publisher's Note** Springer Nature remains neutral with regard to jurisdictional claims in published maps and institutional affiliations.